Waveform inversion of blended data: How does data blending influence different scales of the velocity model?

Joseph Jennings

ABSTRACT

I explore direct imaging of blended data via linearized and non-linear waveform inversion and how cross-talk artifacts from data blending influence different scales of the velocity model. I first examine the back-scattered component of the velocity model by analyzing the Gauss-Newton Hessian matrix of conventional and blended linearized-waveform inversion. I then look at the tomographic component of the velocity model by computing the gradients of both conventional and blended full-waveform inversion. In both back-scattered and tomographic cases, wavenumber spectra show that high-wavenumber components are more adversely affected due to data blending. Regardless of this loss information, I show on a synthetic dataset that with iteration, accurate and interpretable models can recovered.

INTRODUCTION

Simultaneous source (blended) acquisition is becoming increasingly more mainstream for acquiring large, exploration-scale reflection seismic data sets. This is especially true for ocean-bottom node acquisition. In fact, in some energy companies, it is becoming the case in which one must make the case to management as to why the acquisition should not involve simultaneous sources (Hoelting, 2018). Therefore, it is crucial we understand how to obtain reliable and high-quality seismic images from these data for interpretation and further analysis.

Two approaches exist for imaging data obtained from a simultaneous source survey. The most common approach is to separate the blended data to create data that would have been recorded had the sources not been blended. Once these data are on hand, traditional seismic data processing workflows can be followed in order to make a subsurface image. The other, less-common approach is to bypass the source separation and directly image the blended data. Within recent years, this approach is gaining popularity and in fact in many cases the blended data become part of what is known as a "fast-track" velocity model building workflow in which full-waveform inversion (FWI) is performed directly on the blended data (Hoelting, 2018). The biggest challenge with this approach of direct imaging blended data are the artifacts that appear due to the cross talk between blended sources. (Jiang et al., 2010)

To mitigate the artifacts obtained from directly imaging blended data, Tang et al. (2009) showed that with inversion, rather than just a single pass migration, many of the artifacts will be removed. The reason for this is because when solving an inversion problem, we attempt to recover a subsurface model which does not contain the non-physical events created from the blended imaging. Therefore, as the model is updated with iteration, these non-physical events do not explain the data and are suppressed. However, there still remain many unanswered questions with regards to directly inverting these data. For example, given current blending schemes, how many sources can we blend together before we need to resort to advanced regularization schemes or significantly alter the standard waveform inversion scheme? Additionally, most, if not all published studies have focused on the linearized waveform inversion (LWI) problem, what is commonly referred to as least-squares reverse time migration (LSRTM). The wavenumber components of the subsurface that can be resolved from this inversion form an annulus with a width that is determined by the temporal bandwidth of the data. Full-waveform inversion, however, when applied to data with diving waves is able to begin to fill-in this annulus with what has been called the tomographic component of the subsurface model (Biondi et al., 2017). In this report, I investigate which wavenumber components are most adversely affected due to the cross-talk artifacts.

The remainder of this report is organized as follows: I first revisit the cross-talk artifacts that occur from blended imaging by mathematically deriving the gradient of FWI of blended data. Then, I explore the back-scattered component of the velocity model that is recovered from imaging the primary reflections. I do this by examining the waveform-inversion Gauss-Newton hessian matrices for both blended and conventional data. By looking at the point-spread functions in both spatial and wavenumber domains and by plotting the diagonal of each of these Hessians, I illustrate the differences in the back-scattered components that can be resolved using the different datasets as well as the illumination. Then, I look at the tomographic component of the velocity model by calculating the FWI gradient for a transmission experiment. For both the back-scattered and tomographic components, I show the cross-talk artifacts more adversely affect the higher wavenumber components of the velocity model. Finally, I show both LWI and FWI examples on the Marmousi model in which I blend eight simultaneous sources. For both cases, while some high wavenumber noise is introduced into the model, accurate and interpretable models are reconstructed in spite of the large extent of blending.

THEORY

Blended modeling

For all of my derivations, I consider only the constant density scalar acoustic wave equation with its boundary condition and two initial conditions

$$m(\mathbf{x})\frac{\partial^2 p(\mathbf{x},t)}{\partial t^2} - \nabla^2 p(\mathbf{x},t) = \delta(\mathbf{x}-\mathbf{x}_s)f(t), \tag{1}$$
$$p(\mathbf{x},0)=0, \quad \frac{\partial p(\mathbf{x},0)}{\partial t}=0, \quad p(\mathbf{x}=\infty,t)=0.$$

where $p(\mathbf{x},t)$ is the pressure wavefield, $m=1/c^2(\mathbf{x})$ is the slowness squared and $f(t)$ is a source time function. A simple modification to equation 1 can be made to express blended modeling

$$\frac{1}{c(\mathbf{x})^2}\frac{\partial^2 \widetilde{p}(\mathbf{x},t)}{\partial t^2} - \nabla^2 \widetilde{p}(\mathbf{x},t) = \delta(\mathbf{x}-\mathbf{x}_{s_1})f_1(t) + \delta(\mathbf{x}-\mathbf{x}_{s_2})f_2(t), \tag{2}$$

where $\widetilde{p}=p_1+p_2$ and is known as the blended source wavefield. Note that in general $f_1(t)$ and $f_2(t)$ will be shifted in time and that a blended source wavefield will consist of more than just two sources. In this report, for simplicity, I consider the special case in which only two sources fire at the same time.

Inversion of blended data

In order to estimate the acoustic wavespeed from blended data, I can setup the following PDE-constrained optimization problem

$$\begin{aligned}
&\underset{m(\mathbf{x})}{\text{minimize}} \quad F(\widetilde{p}(\mathbf{x},t),m(\mathbf{x})), \quad \text{where} \\
&F(\widetilde{p},m(\mathbf{x})) = \frac{1}{2}\int_0^T\int_\Omega \left(\widetilde{p}(\mathbf{x},t)-\widetilde{p}_{\text{data}}(\mathbf{x}_r,t)\right)^2\delta(\mathbf{x}-\mathbf{x}_r)dt \\
&\text{subject to} \quad m\frac{\partial^2\widetilde{p}}{\partial t^2} - \nabla^2\widetilde{p} = \delta(\mathbf{x}-\mathbf{x}_{s_1})f_1(t) + \delta(\mathbf{x}-\mathbf{x}_{s_2})f_2(t),
\end{aligned} \tag{3}$$

where $\widetilde{p}_{\text{data}}=\widetilde{p}_{\text{data}_1}+\widetilde{p}_{\text{data}_2}$ and is the recorded blended data and $\widetilde{p}$ is the modeled (predicted) blended data. Note that I am assuming stationary receivers as is typical in ocean-bottom seismic acquisition. Using the adjoint method, we can then derive the adjoint PDE and the gradient of this misfit functional. I leave out the details of this derivation, but we find that the adjoint PDE can be written as

$$m\frac{\partial^2\widetilde{\lambda}(\mathbf{x},\tau)}{\partial\tau^2} - \nabla^2\widetilde{\lambda}(\mathbf{x},\tau) = -(r_1(\mathbf{x},T-\tau)+r_2(\mathbf{x},T-\tau))\delta(\mathbf{x}-\mathbf{x}_r), \tag{4}$$
$$\widetilde{\lambda}(\mathbf{x},0)=0, \quad \frac{\partial\widetilde{\lambda}(\mathbf{x},0)}{\partial\tau}=0, \quad \widetilde{\lambda}(\mathbf{x}=\infty,\tau)=0.$$

where $\widetilde{\lambda}(\mathbf{x},\tau)$ is the adjoint wavefield, $\tau = T - t$ (the reversed-time coordinate), and $r_1 = p_1 - p_{\text{data}_1}$ and $r_2 = p_2 - p_{\text{data}_2}$ (the data residuals). Note that from equation 4, it is clear that as we have a blended forward wavefield, we also will have a blended adjoint wavefield, i.e., $\widetilde{\lambda} = \lambda_1 + \lambda_2$ where λ_1 is the adjoint wavefield due to adjoint source r_1 and λ_2 is the adjoint wavefield due to the adjoint source r_2. With this definition of the adjoint wavefield, I can now express the gradient of equation 3 as follows

$$\frac{\delta F}{\delta m(\mathbf{x})} = \int_0^T \widetilde{\lambda}(\mathbf{x}, T-t)\frac{\partial^2 \widetilde{p}(\mathbf{x},t)}{\partial t^2}dt. \tag{5}$$

Letting $\widetilde{p} = p_1 + p_2$ and $\widetilde{\lambda} = \lambda_1 + \lambda_2$ we can expand the gradient as

$$\frac{\delta F}{\delta m(\mathbf{x})} = \int_0^T \lambda_1\frac{\partial^2 p_1}{\partial t^2} + \lambda_2\frac{\partial^2 p_2}{\partial t^2} + \lambda_1\frac{\partial^2 p_2}{\partial t^2} + \lambda_2\frac{\partial^2 p_1}{\partial t^2}dt. \tag{6}$$

Equation 6 describes the gradient of equation 3 with respect to slowness-squared. Note that this gradient is nearly the same as the traditional FWI gradient in which we have the sum of the gradients from each shot (the first two terms in equation 6) but we have some additional cross terms due to data blending. These pesky cross terms cause non-physical artifacts to appear in the FWI gradient. In the following section, I will illustrate with some numerical examples how these artifacts influence the different scales of the gradient calculation. This in turn will describe how these artifacts affect the performance of both FWI and LWI.

NUMERICAL EXAMPLES

To understand better the influence of the cross-terms that appear in the waveform inversion gradient on different scales of the velocity model, I first look at the back-scattered component of the model that is created from imaging primary reflections. As the Gauss-Newton Hessian of the FWI objective function provides all necessary information about the imaging system (for a given acquisition geometry and velocity model) (Valenciano, 2008) it will be a necessary tool for observing the effects of data blending. Therefore, an analysis of the Gauss-Newton Hessian can provide useful insights with regards to linearized imaging of blended data and will illustrate how the back-scattered component of the velocity model is influenced by data blending.

To explore the tomographic component of the velocity model, or rather, the component of the velocity model that can be reconstructed via transmission or after the first iteration of FWI (i.e., multiple scattering within surface reflection data), I will look at the FWI gradient for a transmission experiment conducted on a simple model based on a model originally presented by Mora (1989). With this simple model, I show the effects of data blending on the tomographic component of the model in the wavenumber domain.

Lastly, I perform LWI and FWI on the Marmousi model. In both cases, I used eight sources to create each blended source. I show that with 100 iterations of linear conjugate gradient and with 120 iterations of LBFGS, I can reconstruct accurate and interpretable models.

Backscattered component: Gauss-Newton Hessian from blended data

To understand how the artifacts from the cross-terms map into our migrated image, I first look at a simple example of a homogeneous model with two sources and one receiver. The sources were placed at 400 and 600m and the receiver was placed at 1500m. Figure 1 shows the acquisition geometry. I calculated the full Gauss-Newton Hessian for this imaging scenario. Figure 2 shows the comparison of one column of the Hessian in which the two sources are not blended and in which they are blended.

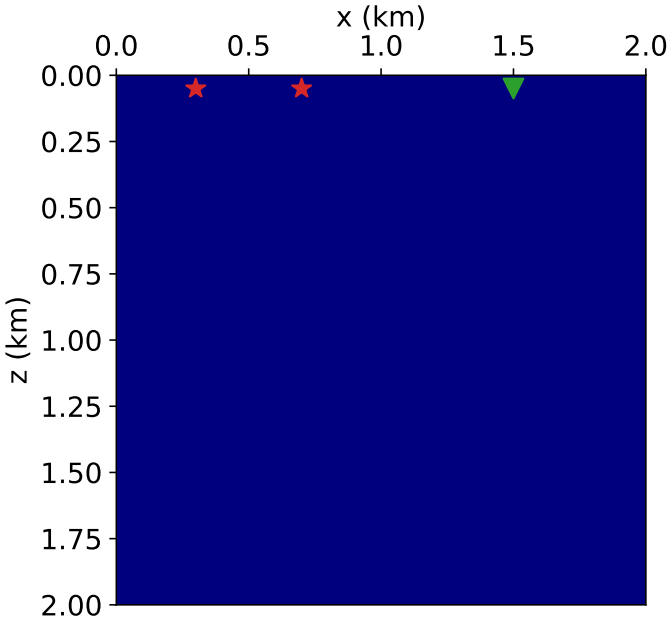

Figure 1: Acquisition geometry plotted on velocity model for first Hessian calculation. Red stars indicate source positions and green triangles indicate receiver positions. [**ER**]

Note in panel (a), we observe two migration ellipses and that they intersect at the position of the point scatterer that was used to compute this column of the Hessian. As explained by equation 6, we observe this event in the column of the blended Hessian but we also observe two additional events that are due to the cross-terms. Note that these terms are of nearly the same magnitude as the true event. Figure 3 shows the comparison of the diagonals of the Hessian matrices for the same imaging scenarios. Note that the diagonals of both Hessians are nearly identical which indicates for this imaging scenario the diagonal of the blended Gauss-Newton Hessian is largely unaffected by the cross talk. This means that for both scenarios there is virtually no difference in illumination.

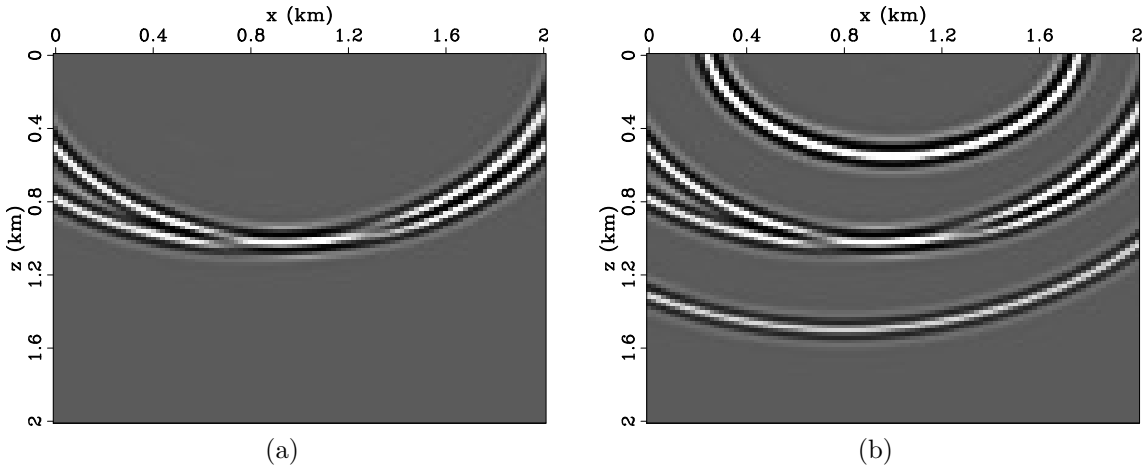

(a) (b)

Figure 2: One column of (a) the Gauss-Newton Hessian matrix for two unblended sources and one receiver and (b) one column of the Gauss-Newton matrix for one blended source (two sources) and one receiver. Note the clear presence of the cross-talk between sources in panel (b). [**CR**]

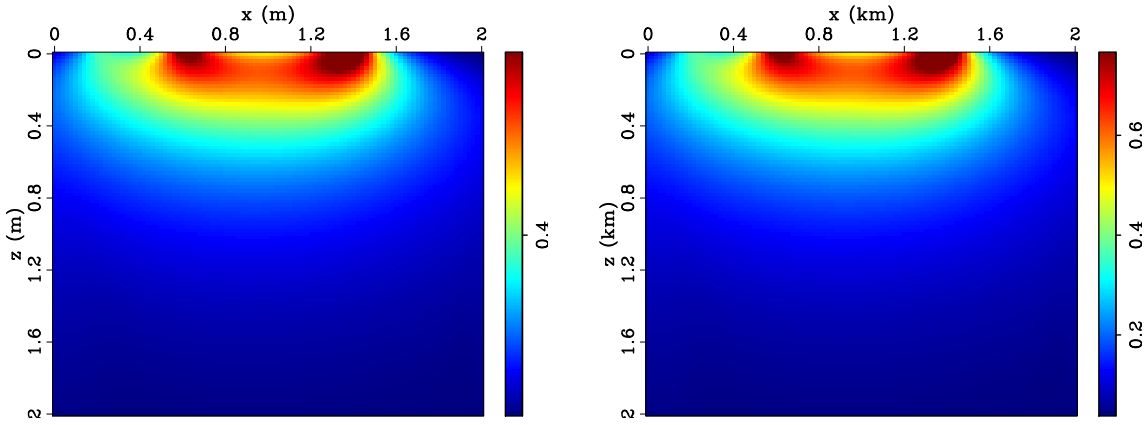

(a) (b)

Figure 3: Diagonal of (a) the Gauss-Newton Hessian matrix for two unblended sources and one receiver and (b) the diagonal of the Gauss-Newton Hessian matrix for one blended source (two sources) and one receiver. In spite of the cross talk seen previously, for this imaging scenario, the diagonal of the blended Hessian appears largely unaffected. [**CR**]

I then performed the same calculations but for the case of 101 receivers positioned at the surface with 20 m spacing and 50 sources placed at every 40 m. The acquisition geometry for this experiment is shown in Figure 4. The blended Hessian was created from blending two sources at the same time and each source was spaced 400 m apart. Additionally, uniformly distributed random time delays between 0 and 0.6 s were applied to each source time function. Figure 5 shows the comparison of one column the unblended and blended Gauss-Newton Hessians for these imaging scenarios.

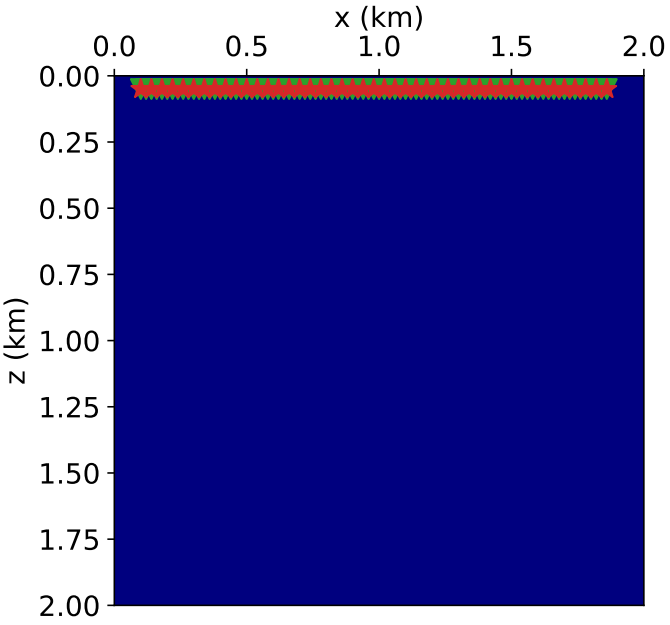

Figure 4: Acquisition geometry for second experiment plotted on the velocity model. 50 sources and 101 receivers were positioned at the surface of the model. Red stars indicate source positions and green triangles indicate receiver positions. [**ER**]

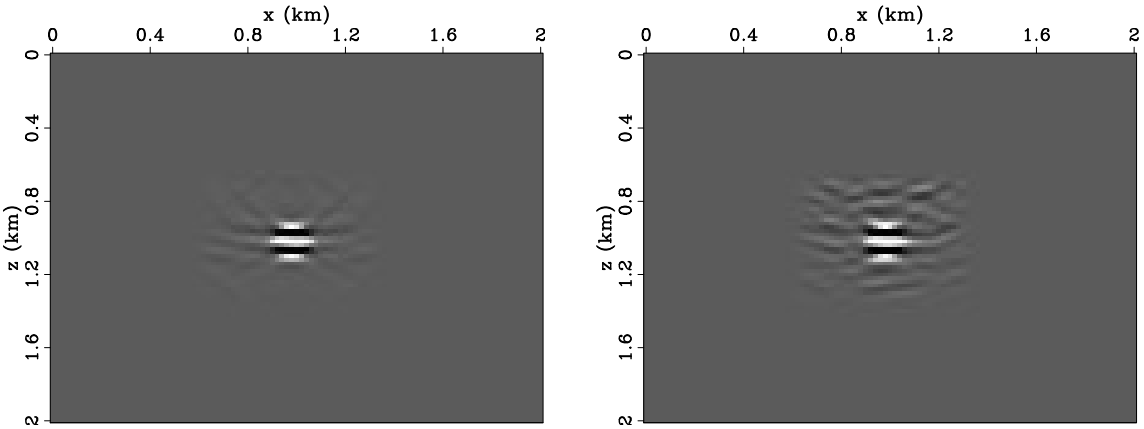

Figure 5: One column of (a) the Gauss-Newton Hessian matrix for 101 receivers and 50 unblended sources and (b) one column of the Gauss-Newton Hessian matrix for 25 blended sources (50 total sources) and 101 receivers. [**CR**]

Note that while both columns have energy localized at the diagonal, it is clear from Figure 5b that blending does introduce larger off-diagonal terms in the Hessian matrix.

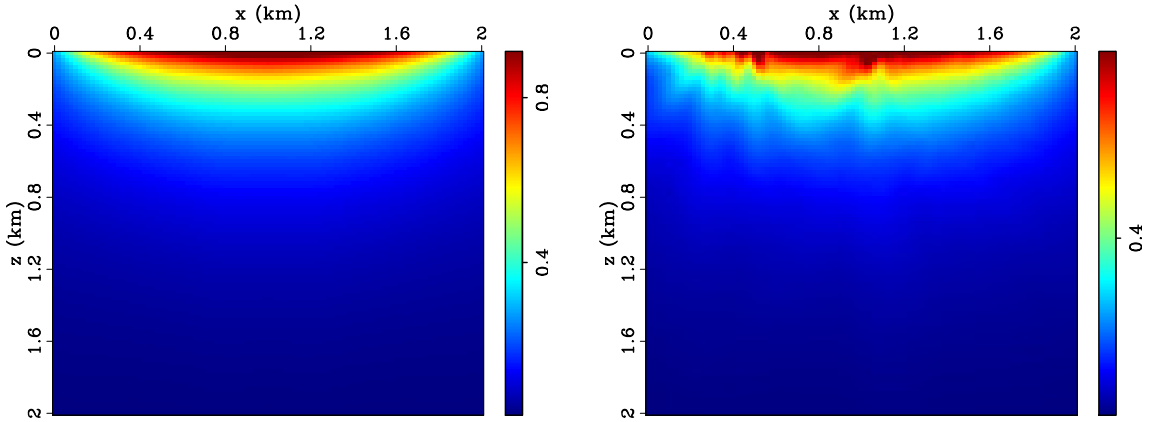

(a) (b)

Figure 6: Diagonal of (a) the Gauss-Newton Hessian matrix for 101 receivers and 50 unblended sources and (b) one column of the Gauss-Newton Hessian matrix for 101 receivers and 25 blended sources (50 total sources) [**CR**]

Additionally, for this imaging scenario, the diagonal is also affected by the introduction of simultaneous sources as is shown in Figure 6. Figure 6a shows the illumination that we expect for a homogeneous velocity model and a symmetric, dense surface acquisition. In contrast, when blending is introduced, we can observe irregularity in the illumination of the subsurface. The reason for this is that the cross-terms are strong enough to influence the diagonal. In the first case, the blending was performed such that cross-terms never affected the diagonal.

For a final and perhaps most meaningful experiment with the blended Gauss-Newton Hessian, I extended the offset from two to ten kilometers and extended the depth to three kilometers. This resulted in a total of 501 receivers with 20 m spacing and 51 sources with 200 m spacing. I also significantly increased the blending so that of the 51 sources, I had three blended sources, one with 17 sources, another with 19 and the last with 15 unblended sources. The acquisition geometry for this experiment is shown in Figure 7. One column from each of the Hessian matrices from these experiments is shown in Figure 8. Note that with the increase in offset, the local Hessian operator has different characteristics than what was shown in Figure 5. Perhaps the most noticeable difference is the long-wavelength component that spans laterally across the model through the point-spread function. Also, due to the dramatic increase in blending, the off-diagonal elements are of much greater magnitude than in previous examples.

In addition to viewing the column of the Hessian in the spatial domain as I have shown previously, it is also useful to see what wavenumber components of the model that can be imaged by looking at the k-space (wavenumber domain) representation of the column of the Hessian as is shown in Figure 9. Firstly we observe the k-space response in this figure matches closely with what has been shown theoretically using Fourier acoustics (Wu and Toksöz, 1987; Mora, 1989). The classical "eye-glasses" are readily

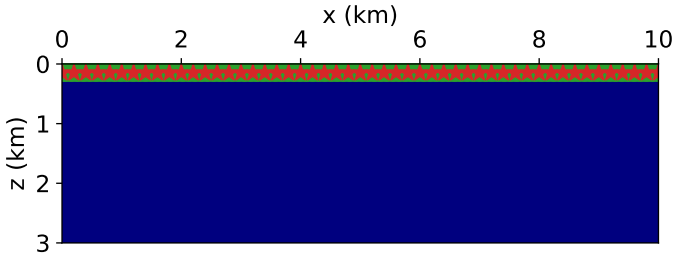

Figure 7: Acquisition geometry for final surface experiment. 51 sources with 200 m spacing along with 501 receivers with 20 m spacing were used. Red stars indicate source positions and green triangles indicate receiver positions. [**ER**]

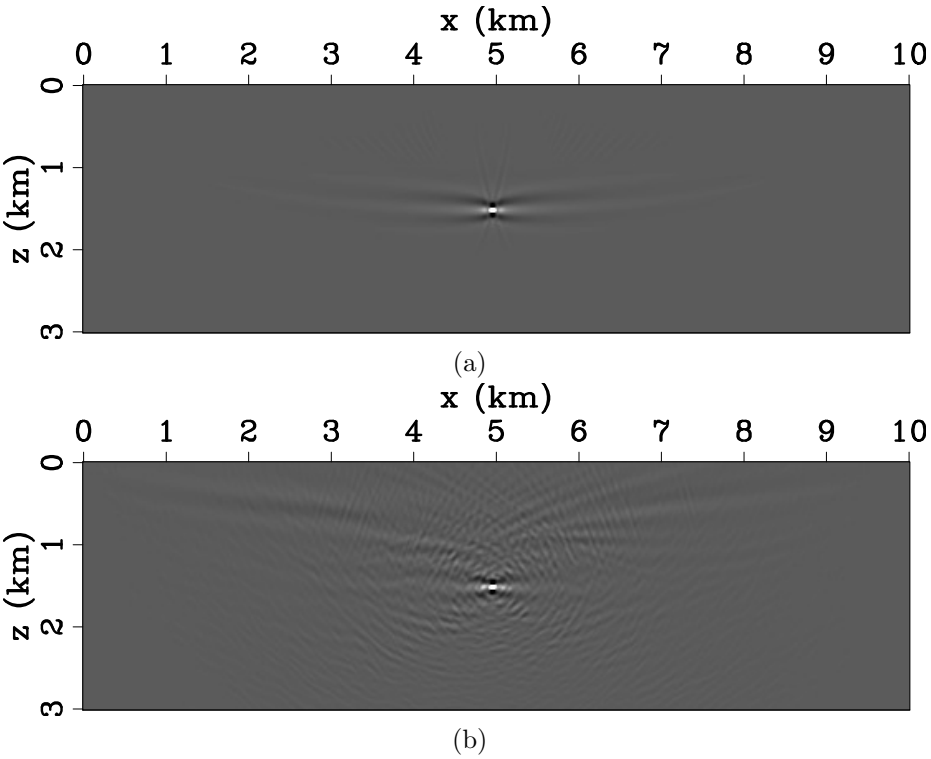

Figure 8: Column of (a) the Gauss-Newton Hessian matrix for 501 receivers and 51 unblended sources and (b) one column of the Gauss-Newton Hessian matrix for 501 receivers and 3 blended sources (17, 19 and 15 unblended sources made up each blended source respectively). [**CR**]

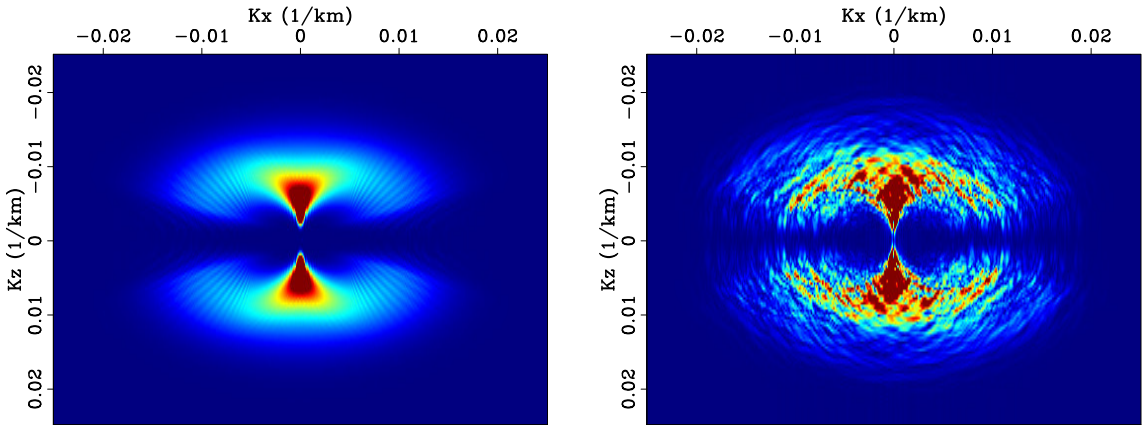

(a) (b)

Figure 9: Wavenumber domain representation of panels (a) and (b) of Figure 8. [**CR**]

apparent and illustrate what components of the subsurface model we can recover from reflection seismic data. Additionally, we observe in the blended k-space response (Figure 9b) that there are notches scattered throughout the spectrum. This indicates that by introducing blended sources, not all components can be correctly recovered. Another insight that we can take from Figure 9 is that different components of the model will be affected differently due to the introduction of data blending. Notice also in Figure 9 that the portion of the k-space response that is controlled mostly by long-offset data (low k_x and $k_z \approx 0 - 0.01$ 1/km) is more uniform than other components of the model that are due to back-scattered energy (see Biondi et al. (2017); Wu and Toksöz (1987); Mora (1989) for more information on the k-space response of a seismic imaging operator).

While the notches in the k-space response of blended Hessian suggest that even with inversion, those components of the model cannot be recovered, Figures 10 and 11 show otherwise. Figure 10 shows one column of the unblended and blended inverse Gauss-Newton Hessians. I inverted the Hessian using 50 iterations of conjugate-gradient least-squares inversion. Note that both inverse Hessians are largely diagonally dominant and while there does exist some noise in the blended inverse Hessian, the off-diagonal elements are very minimal. Figure 11 show the k-space responses for both inverse Hessians. Note that by inverting the Hessian, we are able to fill-in those notches shown in Figure 9. This indicates that while with blended imaging, not all components of the model can be illuminated, much of the loss of illumination can be compensated for by inverting the Hessian.

Tomographic component: FWI gradient from blended data

To explore the tomographic component of the velocity model, I create a transmission experiment. The acquisition of this experiment is shown in Figure 12 and is the same

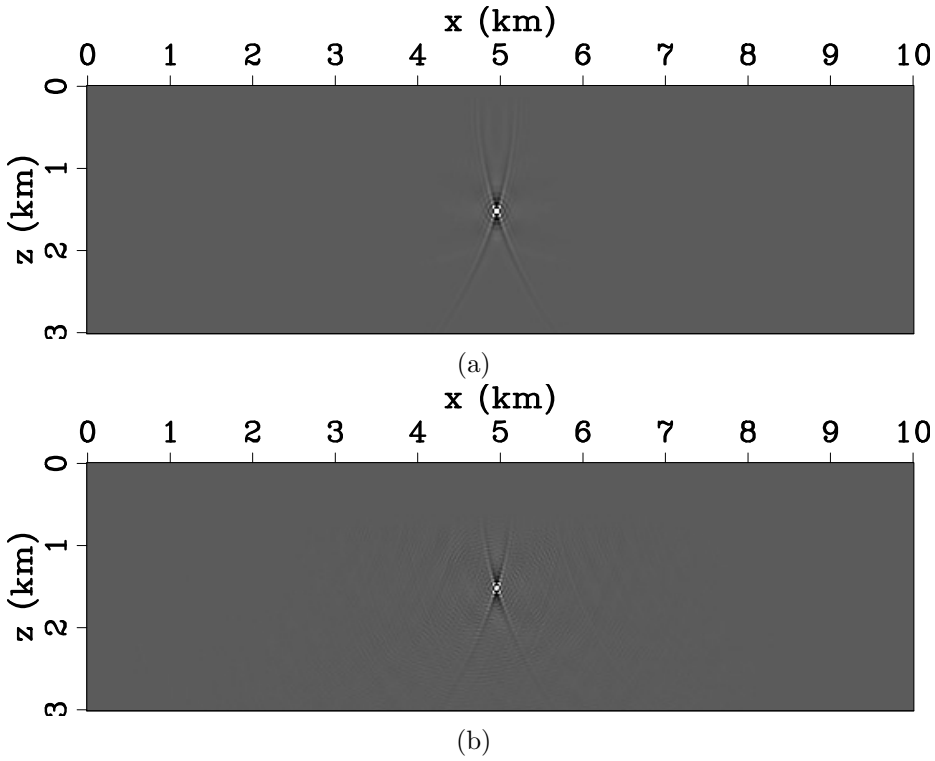

Figure 10: Column of inverse (a) Gauss-Newton and (b) Blended Gauss-Newton Hessian matrices after 50 iterations of conjugate-gradient inversion. The acqusition and blending parameters are the same as described for Figure 8. [**CR**]

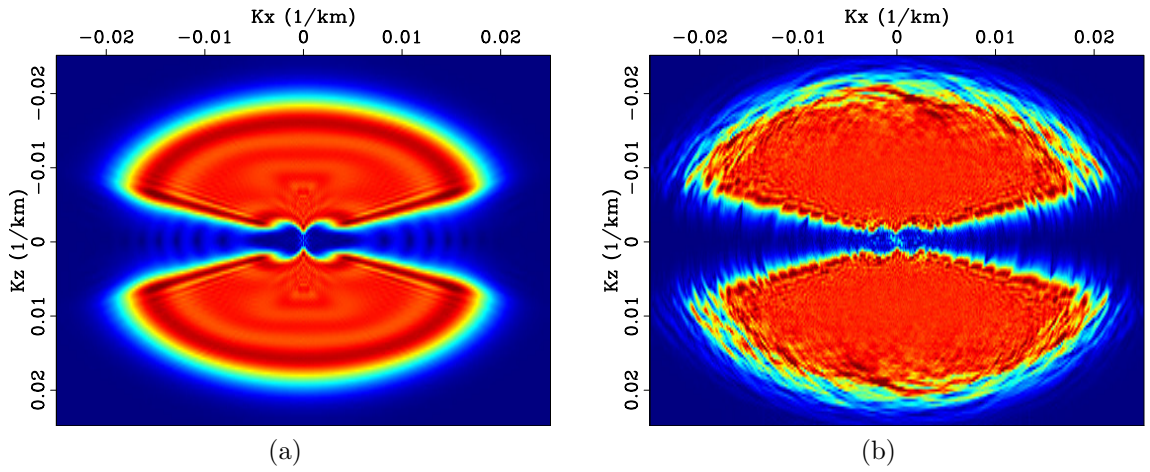

Figure 11: Wavenumber domain representation of panels (a) and (b) of Figure 10. [**CR**]

as Figure 7 but with the receivers at a depth of 3 km. Figure 12 also shows the subsurface velocity model used to model the data. Note that the model is homogeneous apart from a small low-velocity anomaly positioned at the center of the model.

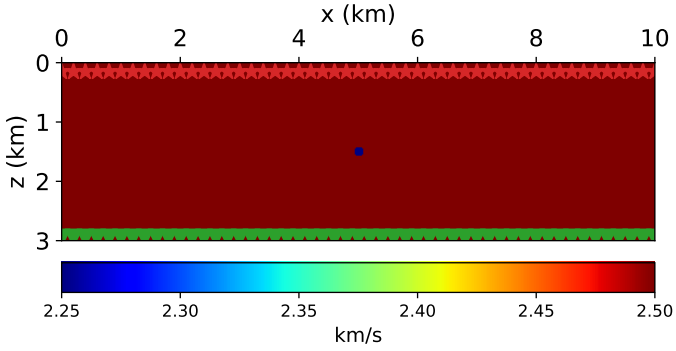

Figure 12: Acquisition setup of transmission experiment. Red stars indicate source positions and green triangles indicate receiver positions. [**ER**]

To examine the influence of data blending on the tomographic component of the model, I modeled data using a homogeneous velocity for both blended and unblended cases. The blended case was created with the exact same blending scheme as was used to calculate Figure 8. The FWI gradients for both the unblended and blended data are shown in Figure 13. As expected, the gradient calculated from blended data appears as the unblended gradient but with some noise.

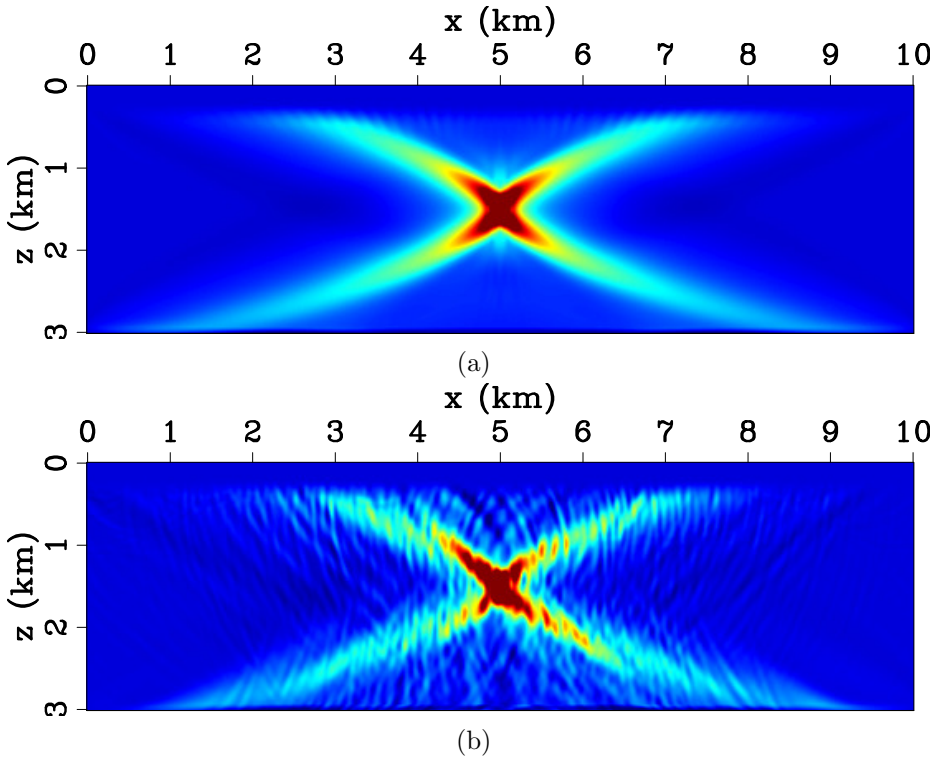

Figure 13: FWI gradients for the transmission problem shown in Figure 12. (a) The FWI gradient for unblended data and (b) the FWI gradient for blended data. In both cases, the initial model was a homogeneous model of 2.5 km/s. [**CR**]

As in the previous section, to observe the influence the blending on the tomographic component, I look at the k-space response of the gradients shown in Figure 13. First I observe that as with the surface reflection experiment, the plots agree well with what is theoretically predicted by Fourier acoustics (Wu and Toksöz, 1987). In fact, they essentially form the complement of what is shown in Figure 9. Also, it is clear in Figure 14b that severe notches have formed in the spectrum and that again the notches appear at the higher wavenumbers rather than the low wavenumbers.

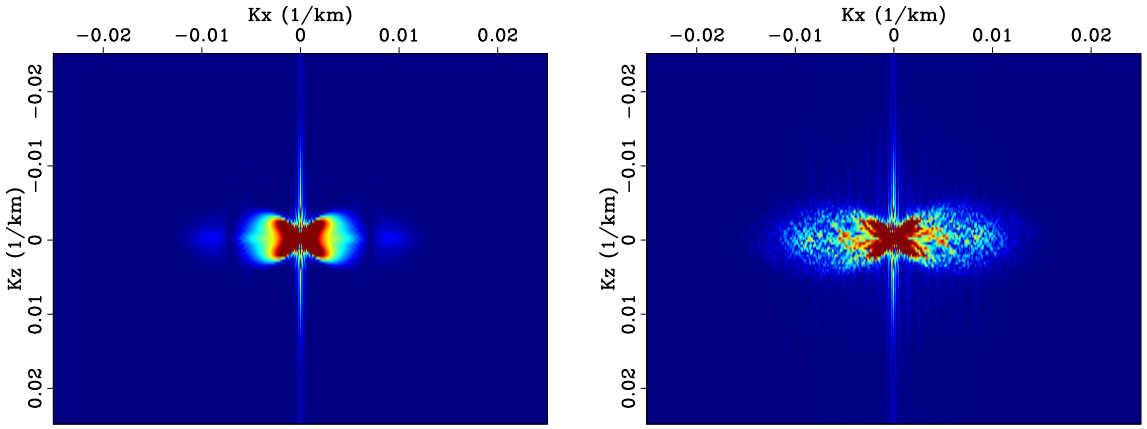

Figure 14: k-space representation of FWI gradients shown in Figure 13. [**CR**]

Figure 15 shows the result of six iterations of FWI starting from a homogeneous model of 2.5 km/s. Note that for both blended and unblended data, the anomaly was recovered with minimal artifacts. Figure 16 shows the k-space response of both inverted results. Like in the back-scattered component case, the inversion is able to fill-in many notches that were present in the original gradient. Also, while the lower wavenumber components are largely intact, there is some obvious noise present in the higher wavenumbers.

Marmousi model

I now present some results of both LWI and FWI of blended data created using the synthetic Marmousi model. Figure 17 shows the background acoustic wavespeed (migration velocity) model used for all LWI results. Figure 18a shows the result of 100 iterations of LWI with 48 sources with 200 m spacing and 471 receivers with 20 m spacing. The linearized portion of the model has been generally well recovered. Figure 18b shows the LWI result but now for blended data in which eight sources were blended each being made up of six unblended sources. Random time delays were applied to each source time function in order to simulate a shot time dither. Note that apart from weak high wavenumber noise at the bottom of the model, the two results appear nearly identical.

Figure 19 shows the result of performing 120 iterations of FWI on synthetic data

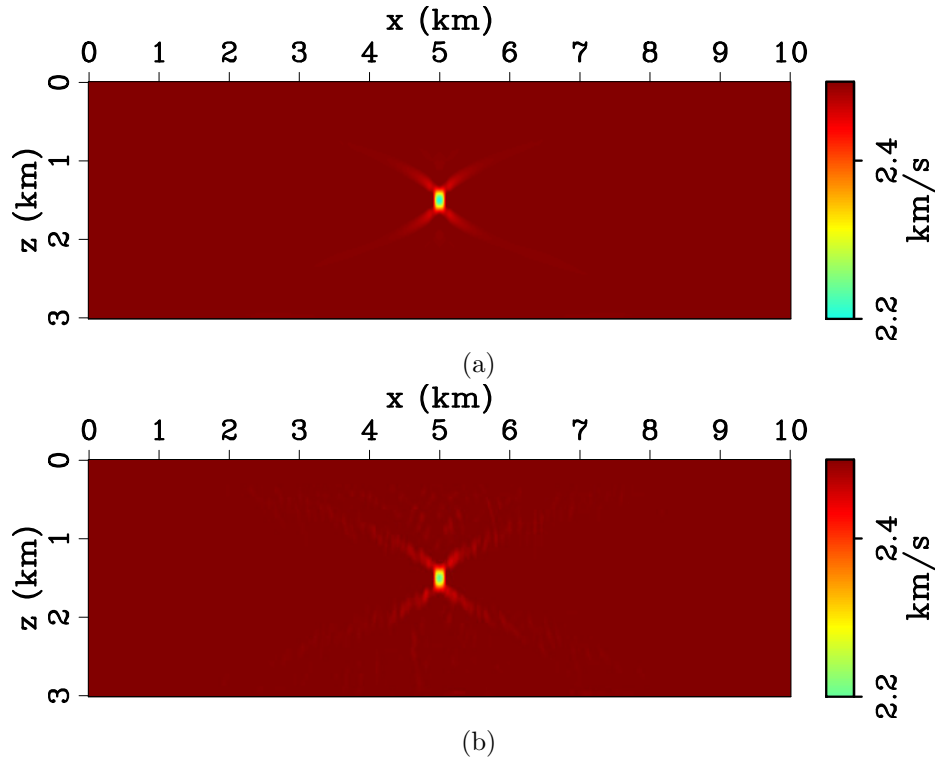

Figure 15: Results of FWI inversion of small point anomaly starting from an initial model of 2.5 km/s. Panel (a) shows the inverted result after 6 iterations of FWI of unblended data using LBFGS. Panel (b) shows the same but for blended data. In both figures, the original model has essentially been recovered. [**CR**]

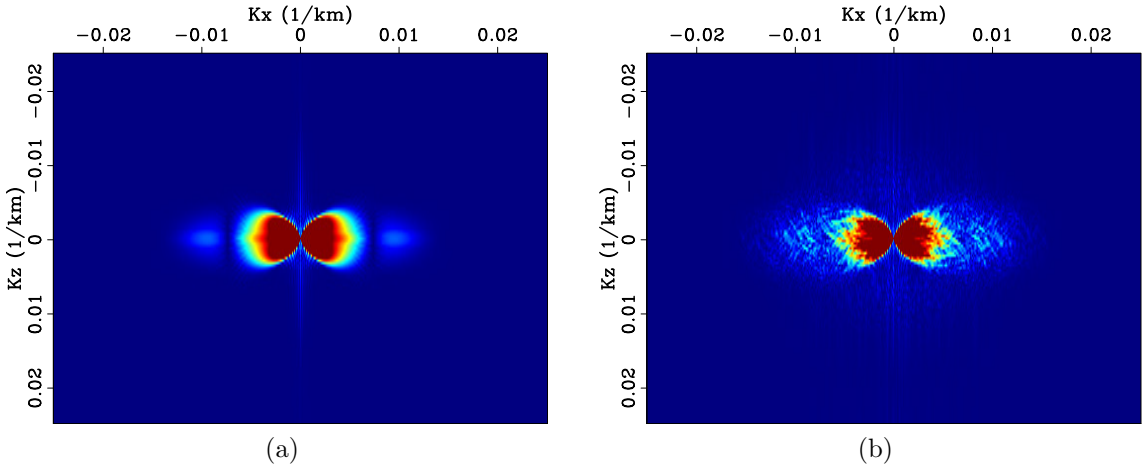

Figure 16: k-space representation of inverted models shown in Figure 15. [**CR**]

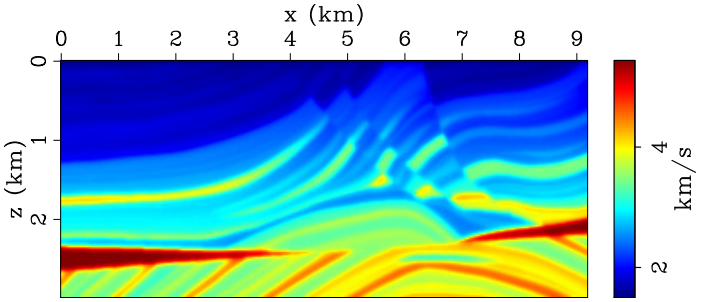

Figure 17: Background model used for linearized inversions. [**ER**]

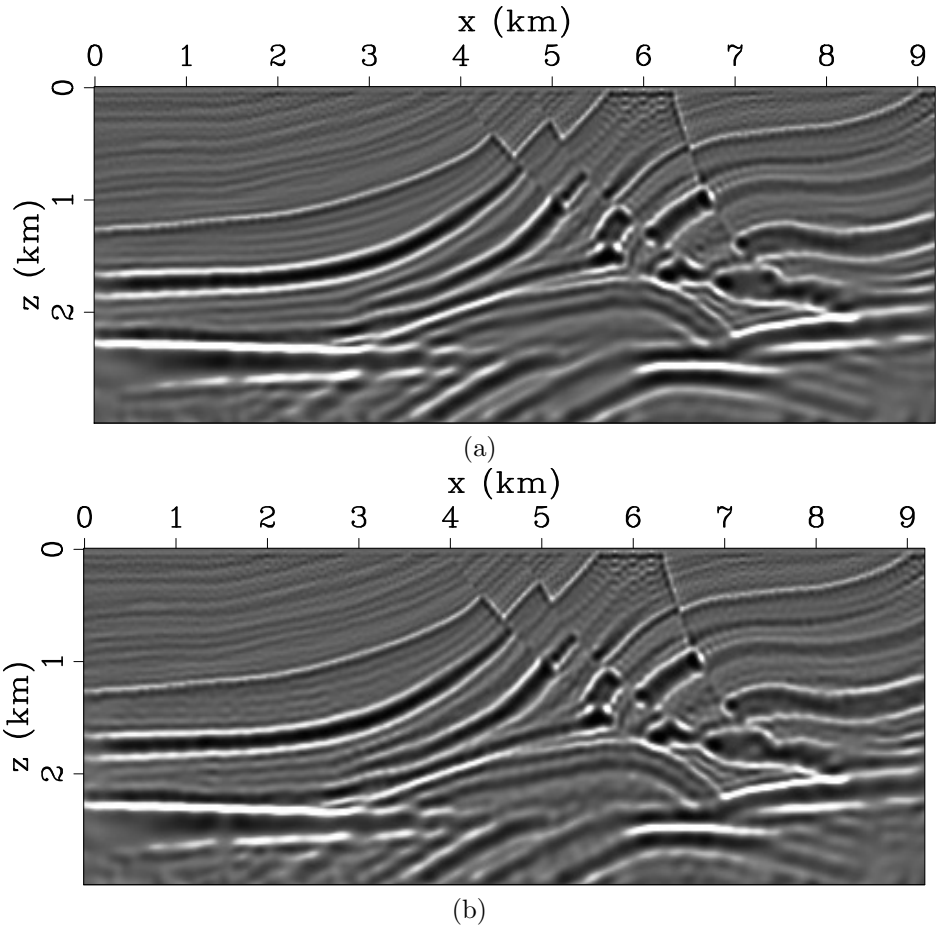

Figure 18: Results of 100 iterations of LWI of unblended and blended data from the Marmousi model. (a) LWI on unblended data and (b) blended LWI using where each blended source consisted of 6 unblended sources. [**CR**]

modeled from the Marmousi model. Figure 19a shows the initial model which is just a smoothed version of the true model. Figure 19b shows conventional FWI performed on unblended data. The data had the same acquisition as was performed for the LWI example. The wavelet used was a zero-phase wavelet with frequencies from 0-15 Hz. Note that after 120 iterations, most components of the model have been well-recovered. Figure 19c shows the result of the same number of iterations of FWI but for a simultaneous source acquisition. The blending scheme as the same that was used for the LWI example. Note that apart from some short-wavelength noise, the model has been well-recovered in spite of the large amount of blending present in the shot gathers.

These results of LWI and FWI on the Marmousi model indicate that in the presence of simultaneous source interference, accurate/interpretable models can be recovered. They also agree with the k-space responses shown in Figures 11 and 16 which indicate that regardless of large notches that appear in the waveform inversion gradient and Hessian, iterative inversion seems to fill these notches in. These Marmousi examples show that this is true even in the presence of large amounts of blending and for highly complex subsurface models.

CONCLUSION

I investigated the question of how does data blending influence different scales of the velocity model? I looked at both back-scattered and tomographic components of the model. I did this with two experiments. One involved calculating the Gauss-Newton Hessian and its inverse for a surface experiment. The other involved calculating the FWI gradient for a point anomaly and then recovering the anomaly from unblended and blended data. Both experiments showed that the cross-talk artifacts appear to equally influence both the back-scattered and tomographic components: they introduce notches in the wavenumber spectrum at high wavenumbers. From the results shown in this report, I cannot yet say whether the backscattered component or the tomographic component is more adversely affected by data blending but it appears as if it is the same for both scales. Perhaps surprisingly, I also showed that inversion is able to fill in these notches over iteration and that in spite of a large number of blended sources, accurate models can be reconstructed. Numerical experiments performed on the Marmousi confirm this and show that even eight simultaneous sources, accurate, interpretable models can be recovered. Given the amount of noise seen on these synthetic results, it is conceivable that noise might not even be observed when inverting blended field data. This noise, however, will likely not be negligible when 4D analysis is desired and weak signals must be preserved. (Krupovnickas et al., 2012).

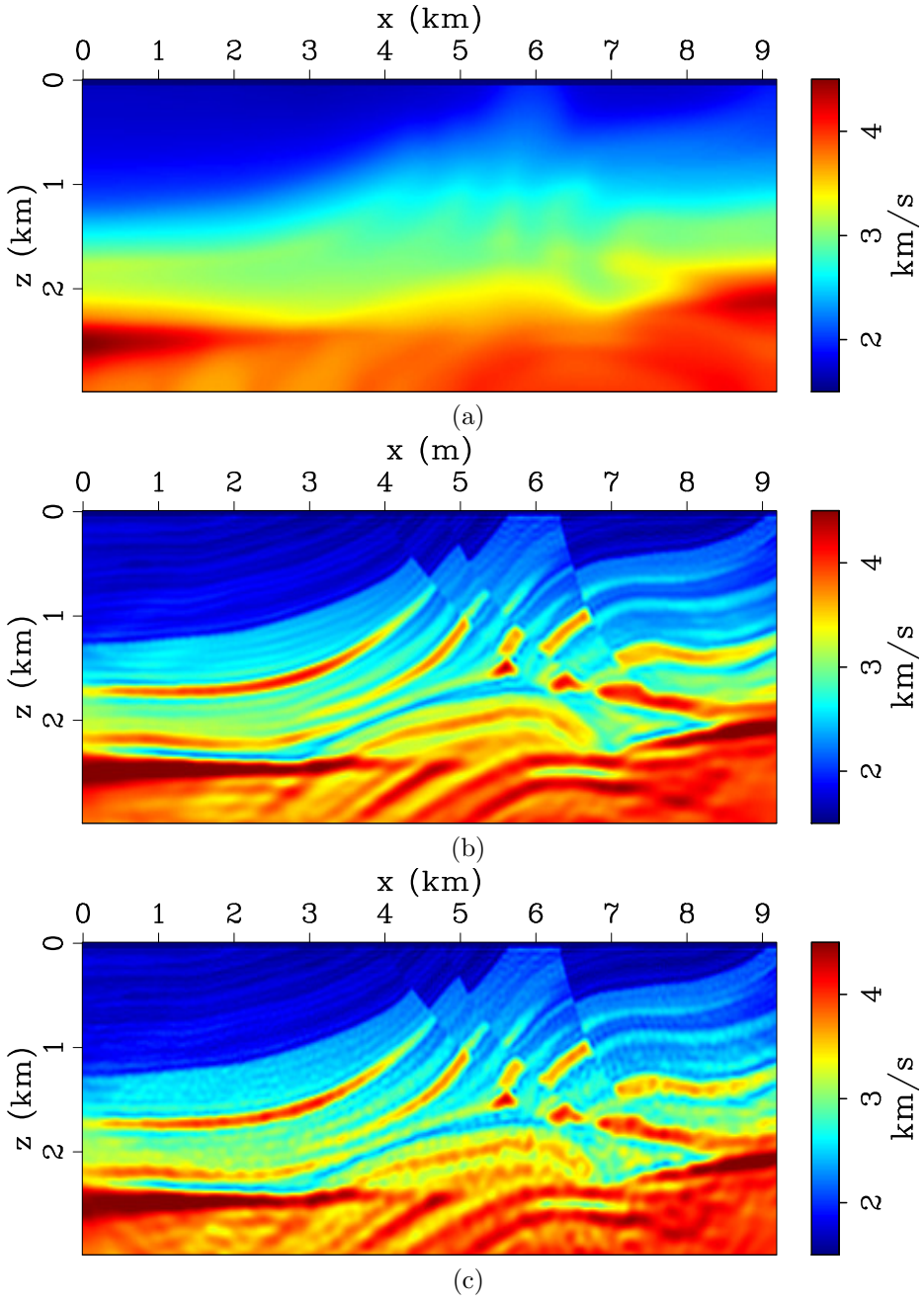

Figure 19: Results of 120 iterations of FWI of unblended and blended data from the Marmousi model. (a) The initial model used for both FWI calculations, (b) FWI on unblended data, (c) blended FWI using where each blended source consisted of six unblended sources. [**CR**]

ACKNOWLEDGEMENTS

I would like to thank Professor Biondo Biondi for advising me to look at the k-space response for a blended imaging operator. I also would like to thank Yinbin Ma for explaining how to efficiently calculate the Hessian.

REFERENCES

Biondi, B., E. Biondi, and G. Barnier, 2017, Can full waveform inversion image all scales of the velocity model? .

Hoelting, C., 2018: personal communication.

Jiang, Z., R. Abma, et al., 2010, An analysis on the simultaneous imaging of simultaneous source data: Presented at the 2010 SEG Annual Meeting, Society of Exploration Geophysicists.

Krupovnickas, T., K. Matson, C. Corcoran, and R. Pascual, 2012, Marine simultaneous source obs survey suitability for 4d analysis, *in* SEG Technical Program Expanded Abstracts 2012: Society of Exploration Geophysicists, 1–5.

Mora, P., 1989, Inversion= migration+ tomography: Geophysics, **54**, 1575–1586.

Tang, Y., B. Biondi, et al., 2009, Least-squares migration/inversion of blended data: Presented at the 2009 SEG Annual Meeting, Society of Exploration Geophysicists.

Valenciano, A. A., 2008, Imaging by wave-equation inversion: PhD thesis, Stanford University.

Wu, R.-S., and M. N. Toksöz, 1987, Diffraction tomography and multisource holography applied to seismic imaging: Geophysics, **52**, 11–25.